This is the Pre-Published Version.

This is the peer reviewed version of the following article: Y. Li, H. Wu, L. Zhuang, W. K. Lai, S. Lin, S. P. Lau, Efficient Optical Control of Quantum Tunneling Devices Based on Layered Violet Phosphorus. Adv. Optical Mater. 2025, 13, 2402720, which has been published in final form at https://doi.org/10.1002/adom.202402720. This article may be used for non-commercial purposes in accordance with Wiley Terms and Conditions for Use of Self-Archived Versions. This article may not be enhanced, enriched or otherwise transformed into a derivative work, without express permission from Wiley or by statutory rights under applicable legislation. Copyright notices must not be removed, obscured or modified. The article must be linked to Wiley's version of record on Wiley Online Library and any embedding, framing or otherwise making available the article or pages thereof by third parties from platforms, services and websites other than Wiley Online Library must be prohibited.

Efficient Optical Control of Quantum Tunneling Devices Based on Layered Violet Phosphorus

Yanyong Li[1,2], Haolong Wu[1], Lyuchao Zhuang[2], Wai Kin Lai[2], Shenghuang Lin[3,], Shu Ping Lau[2,*]*

Dr. Y. Y. Li, H. L. Wu, Dr. L. C. Zhuang, W. K. Lai, Prof. S. P. Lau

[1] Henan Key Laboratory of Quantum Materials and Quantum Energy, School of Quantum Information Future Technology, Henan University, Kaifeng, 475000, Henan, P. R. China

[2] Department of Applied Physics, The Hong Kong Polytechnic University, Hung Hom, Kowloon, Hong Kong SAR, P. R. China

E-mail: apsplau@polyu.edu.hk

Dr. S. H. Lin

[3] Songshan Lake Materials Laboratory, Dongguan, 523808, Guangdong, P. R. China

E-mail: linshenghuang@sslab.org.cn

Keywords: violet phosphorus, photoresponse, tunneling diode, interband tunneling, negative differential transconductance

Abstract

Electron tunneling devices attract attention due to their potential applications in integrated circuits, memories, and high-frequency oscillators. However, limited works are devoted to the optical control of electron tunneling processes. The main reason is the low concentration of photogenerated carriers concerning the equilibrium values in heavy-doped regions. In this work, violet phosphorus (VP) with a unique bi-layer tubular structure supplies an excellent platform for investigating the tunneling mechanisms under photo illumination. A VP-based vertical tunneling diode made of metal-insulator-semiconductor (MIS) stacking is presented. The photogenerated carriers increase the tunneling current by ~4.2 times through photo illumination, leading to a considerable rectification ratio. In addition, a three-terminal tunneling field-effect transistor (TFET) made from VP flake with different thicknesses is also presented. The interband tunneling of electrons results in a tunable negative differential transconductance (NDT) at room temperature. The photo illumination can modulate the onset of the NDT region due to the variation of the density of states with Fermi level alignment in the channel and drain region. Our results advance the understanding of electron transport mechanisms in VP-based tunneling devices, showing great potential for exploiting novel two-dimensional (2D) multifunctional devices with interactions between light and carriers' tunneling.

1. Introduction

With electronic devices persistently scaling down, limited processing speed and high power consumption seriously impede the sustainable development of information technology. Compared to conventional metal-oxide-semiconductor field-effect transistors (MOS-FETs), tunneling devices have the advantages of lower off-state leakage current and subthreshold swing (S), which hold great potential for breaking through the scaling limit.[1, 2] Electron tunneling derives from the quantum effect of electrons in confined systems, which makes electrons with low kinetic energy overcome high potential barriers and form currents. Hence, the performance of tunneling devices is subject to the tunneling probability. Most tunneling devices operate based on the mechanisms of interband tunneling (IBT) and resonant tunneling (RT), which have high operation speed and energy-efficient characteristics.[3, 4] That quantum mechanism leads to the unique peak-valley transport phenomenon of negative differential transconductance (NDT) or negative differential resistance (NDR),[5, 6] which has been exploited broadly in high-efficiency analog and digital electronic applications, such as multivalue devices and high-frequency oscillators.[7-9] However, at the current stage of research, most NDT/NDR devices, like Esaki diodes, Gunn diodes, and single-electron transistors, are fabricated in Si-Ge and III-V semiconductor heterostructures for a lower V_{dd}.[10, 11] Although the traditional bulk semiconductor-based tunneling devices show better working voltages, the formation of various heterostructures is limited by the threading dislocations induced by lattice mismatch at the interfaces. Moreover, the stringent bandgap match in traditional heterostructures hinders the mass production of desired tunneling devices.

In this light, semiconducting 2D materials exhibit significant advantages in novel tunneling devices due to the surface's atomically sharp edges and non-dangling bonds.[12, 13] Furthermore, the feature of van der Waals (vdW) stacking by 2D materials allows different band-edge

alignments with distinct band structures, facilitating the fabrication of NDT/NDR devices with tailed band structures. For example, black phosphorus/molybdenum telluride (BP/$MoTe_2$) heterostructure exhibits observable NDT behavior by constructing a specific straddling band alignment.[14] Moreover, the tunneling transport characteristics in that vdW heterostructure can be controlled by switching the heterostructure type from straddling to straggling. Besides the band structure modulation by electrostatic gate bias, most 2D materials possess extraordinary optoelectronic properties, implying that they can act as photoactive layers in the NDT/NDR devices to tune the electron and hole currents.[15-17] For instance, through modulating the work function of tungsten diselenide (WSe_2) by various dielectric surroundings, Shim *et al.* exhibited a light-triggered NDT ternary inverter based on tungsten diselenide/graphene (WSe_2/Gr) heterostructure.[15] Besides the advantages mentioned above, combining the ultrathin feature and thickness-dependent bandgaps, tunneling devices based on 2D materials are expected to offer more attractive applications in 2D electronics/optoelectronics. Among abundant 2D family, atomically thin VP, a recently discovered 2D material, has shown a unique bi-tubular atomic structure, tunable bandgap (about 1.68~2.02 eV), strong anisotropy, high optical absorption, and good ambient stability.[18] More importantly, the ultralow room temperature dark current (~fA) and tunable ambipolar transport characteristics make it a potential candidate for 2D tunneling devices toward multifunctional electronic/optoelectronic applications.[19, 20] Previous work has reported the prominent NDR effect in black phosphorus (BP), VP's allotrope.[21] However, the weak chemical stability of BP in the ambient prevents it from scalable and durable applications. Despite the remarkable progress in the research of VP, to the best of our knowledge, the underlying carrier transport in VP-based tunneling devices with various configurations is still unclear and needs further exploration.

This work provides an in-depth understanding of the transport properties in vdW layered VP tunneling devices with out-of-plane and in-plane tunneling geometries. The stacking of graphene/hexagonal boron nitride/violet phosphorus (Gr/*h*-BN/VP) flakes constructs a metal/insulator/semiconductor (MIS) vertical tunneling diode with a high rectification ratio of ~650 at room temperature. We also confirm that the electrostatic gate bias and photo illumination can efficiently modulate the electron tunneling behaviors. Furthermore, a VP tunneling field-effect transistor (TFET) with a noticeable NDT feature was also developed based on the in-plane *n*-*p*-*n* homojunction. The NDT phenomenon is achieved by controlling the doping state of the channel component through Ar^+ plasma treatment. In addition, as the layered VP is photoactive, the figures of merit in NDT regions can be tuned by the population of photogenerated carriers by changing the quasi-Femi levels in various components of the TFET. Finally, our results pave the way for practical applications of VP-based tunneling devices in future multifunctional devices.

2. Results and Discussion

Violet phosphorus, as one of the allotropes of elemental phosphorus, is a kind of layered semiconductor with a direct bandgap estimated to be from ~2.02 eV (monolayer) to ~1.68 eV (bulk).[22-25] Unlike the orthorhombic black phosphorus (BP), VP belongs to the monoclinic lattice space group *P2/n* and the atomic structure is more complicated, which consists of a P8 cage, a P9 cage and the bridging P2 dumbbell in a repeating unit as shown in **Figure S1**.[26, 27] The repeating unit constitutes phosphorus tubes with pentagonal cross sections. Through covalently bonded to another phosphorus tube by the roof P atom, a bi-tubular layer is formed with one layer stacked on another perpendicularly along the *z*-direction, as shown in the inset of **Figure 1**a. As reported in our previous work, bulk VP crystal was synthesized by chemical vapor transport (CVT) starting

from red phosphorus, tin, and iodine (Figure 1a).[28] The unique layered feature ensures bulk VP can be exfoliated into few-layer flakes (~30 nm in thickness) easily, as shown in Figure 1b, which has been indicated by the yellow dash-dot lines in the high-resolution transmission electron microscopy (HRTEM) image shown in Figure 1c. Clear parallel phosphorus chains can be observed, suggesting the stacked bi-tubular structure. Raman scattering is a powerful and non-destructive method of identifying the structural properties and crystal quality of 2D materials.[29-31] Figure 1d illustrates the Raman spectrum of VP flakes excited by a 532 nm continuous wave laser in the back-scattering configuration. Compared with BP, plenty of Raman modes are observed, suggesting the low symmetry of the lattice vibration and a higher phonon density of states in VP crystals.[32, 33] Specifically speaking, the Raman modes of VP derive from various vibrations of the basic repeating unit (-[P9]-[P2]-[P8]-). Among these Raman modes, three predominant modes, $S^{2}_{[P9]}$(353 cm^{-1}), $S^{1}_{[P8]}$(359 cm^{-1}) and $S^{2}_{[P8]}$(373 cm^{-1}), originate from the stretching vibration of P9 and P8 cages with the strongest intensities.[34] By contrast, other weak Raman modes in the lower frequency range (< 290 cm^{-1}) mainly result from the integrated deformation of the tubular structure, such as the torsional vibration and asymmetric radial breathing of the tubular structure.[35, 36] The complicated Raman spectrum implies that strong phonon scattering may exist in VP crystals, suggesting a strong light-matter interaction and phonon-electron scattering in VP crystals.[37, 38] PL measurements were conducted at room temperature under a 532 nm laser excitation. The strong light-matter interaction shows obvious PL emission with a maximum emission energy of ~1.91 eV, as depicted in **Figure S3**a. In general, the bandgaps of semiconductors increase due to additional quantum confinement. As for layered materials, the band structure strongly depends on the thickness, reflected by the thickness-dependent variation of PL intensity, as shown in Figure 1e. The corresponding optical microscope

(OM) image is given in the inset. The sharp thickness-dependent colour variation is ascribed to the reflectivity of light from VP flakes with different thickness.[39] The atomic force microscope (AFM) image supports the region's thickness variation, as shown in Figure 1f. It is worth noting that the full width at half maxima (FWHM) of the broad PL peak is nearly 0.23 eV (Figure S3b), much larger than common transition metal dichalcogenides (TMDs).[40-42] It suggests that the PL of the VP flake at room temperature may be a defect-dominated emission rather than a near-edge emission, which has been confirmed in our previous work.[28] Free excitons and trions contribute to the strong and broad photon emission, suggesting that VP is more sensitive to the excitation of visible light than BP and is beneficial for high-performed optoelectronic devices.

Given the strong light-matter interaction in the visible range, we want to explore the optoelectronic performance of intrinsic VP-based phototransistors in ambient conditions without encapsulation. A traditional back-gated phototransistor's OM image is shown in the inset of **Figure 2**a, with the channel thickness of ~30.4 nm confirmed by AFM measurement. Figure 2 illustrates several key figures of merit for the VP-based phototransistors. The drain current I_d is depicted as a function of the bias voltage V_d under $V_g = 0$ V with and without illumination. Benefiting from the strong PL emission in the visible range, the phototransistor was just illuminated by a standard xenon lamp. The dark current reaches ~fA under $V_d = 0.5$ V, implying a considerable sheet resistance of VP flake in the dark. Once illuminated, a remarkable photocurrent was generated by separating the photo-induced electron-hole pairs, resulting in a great ON/OFF ratio of $\sim 2.7 \times 10^2$ at $V_d = 0.5$ V. The superior photoresponse is much larger than that of graphene and BP in the visible range due to the ultralow dark current.[43, 44] The sublinear I-V curve suggests that the Schottky barriers at the ends are negligible for the large photocurrents. Figure 2b shows the transfer curves of the VP phototransistor *w/* and *w/o* illumination at a fixed bias $V_d = 0.5$ V.

The drain current increased gradually when V_g swept from -50 V to 50 V in both conditions, suggesting the *n*-type nature of the obtained VP phototransistors. Notably, the *n*-type doping becomes more serious under illumination, reflected by the negative shift of the charge neutral point (V_{CNP}). The change in the minimum conductivity point is mainly caused by the oxygen-related hole trapping at the surface.[45-48] It suggests that VP exhibits strong oxidation like other allotropes of phosphorus, like BP and fibrous RP.[49, 50] Phosphorus oxidized species (PO_x) on the surface of the VP channels extract equilibrium-free electrons, forming an electron depletion region with a potential direction towards the exterior.[28, 51] Once illuminated, photon-induced holes migrate along the potential and are trapped by the PO_x near the surface. The formula extracts field-effect mobilities at room temperature, $\mu_e = L/(W \cdot C_g) \cdot dG/dV_g$, where L and W are the channel length and width of the phototransistor, respectively; C_g is the gate capacitance per unit area; G is the conductance, and V_g is the applied gate bias.[52] The calculated electron mobilities increase from 2.48×10^{-5} to 6.03×10^{-5} $cm^2\ V^{-1}\ s^{-1}$, resulting in a steeper transfer curve under illumination ($S = 2.7\ V\ dec^{-1}$). The subthreshold swing value is the same magnitude reported in few-layer BP with similar back-gated geometry.[53] The relatively large subthreshold swing may result from the thick dielectric layer of SiO_2 (~285 nm) or the Schottky barriers in the subthreshold regions.[54, 55] The photocurrent's power density dependence was measured at V_d = 1 V and 520 nm laser illumination, as shown in Figure 2c. By fitting the relationship by the power law $I_{ph} = AP_{in}^{\alpha}$, where $I_{ph} = I_{illu} - I_{dark}$ is the photocurrent and A is a constant, the value α was calculated to be ~ 0.73 at room temperature.[56] In particular, the $\alpha$is less than 1 also indicates the existence of trap states. The larger the value of α, the lesser the number of trap states.[57] Notably, the trap states in VP-based phototransistors may originate from several aspects, including the PO_x, structure defects, and substrate interface.[58] Further, we define the responsivity (R) and detectivity (D^*) to evaluate

the devices' photoelectrical performance synergistically by the formula $R = (I_{ph} - I_{dark})/P_{in}S$ and $D^* = A^{*1/2}R/(2qI_{dark})^{1/2}$, where P_{in} is the incident-light intensity, S is the effective illuminated area, A^* is the effective area of the device, and q is the electronic charge, respectively. The R and D^* as a function of the incident light intensity is demonstrated in Figure 2d, which are extracted from Figure 2c at $V_d = 0.8$ V. Clearly, it is found that the R and D^* almost maintain in a high level (R=0.23 mA W^{-1} and $D^* = 1.7 \times 10^{11}$Jones) until the light power increases beyond ~290 mW cm^{-2}. This trend is explained as the increase of recombination possibility at higher illumination level.[59, 60] Next, we further explored the temporal photoresponse at different excitation laser wavelengths (Figure 2e), where the applied $V_d = 0.5$ V, $V_g = 0$ V. Benefiting from the low dark current (~10^{-15}A), the value of photocurrent switch on/off ratio (I_{on}/I_{off}) is estimated to be around 2×10^3 for the 445 nm laser, which is much larger than that of graphene and BP in visible range.[43, 44] Furthermore, the photocurrent saturates quickly once the illumination is on and drops instantly back to the dark current when the illumination is off. To quantificationally exhibit the fast photoresponse of the VP-based phototransistor, the rise (t_R) and decay (t_D) response time were calculated through an exponential fitting, $I = I_0[1 - exp(- t/t_R)]$ and $I = I_0\, exp(- t/t_D)$, where I_0 stands for the maximum saturated value photocurrent under illumination. The t_R and t_D for the 445 nm laser were estimated to be ~ 76.8 ms and ~ 138 ms, respectively, as shown in Figure 2f. Compared with only several milliseconds in BP phototransistors, the slightly longer response time for VP may result from the strong carrier-phonon scattering.[44] Finally, the inset of Figure 2f illustrates that the photoresponse time is proportional to the excitation wavelength. The behaviour suggests that shorter wavelength excitation stimulates the top surface regions. Hence, the surface defects capture the photogenerated holes faster, leading to a shorter response time.

The extraordinary photo-electrical merits of VP-based devices facilitate a broad multifunctional application in 2D electronics and photonics by combining various devices' geometry topologies. Compared with traditional *pn*-junction diodes and MOS-FETs, tunneling devices hold great potential for energy-efficient and multifunctional devices owing to the steep switching feature, ultralow off-current, and unique peak-to-valley transport properties.[5, 61-63] In the following, VP-based tunneling diodes and TFETs thoroughly explore the tunneling mechanisms toward advanced tunneling devices at the 2D limit.

The VP-based vertical tunneling diode was fabricated with the device geometry of metal-insulator-semiconductor (MIS) stacking, as shown in the inset of **Figure 3**a. By employing the dry transfer technique, few-layer graphene acts as the top electrode with an intermediate layer of ultrathin (< 5 nm) *h*-BN as the insulator barrier. Subsequently, another piece of graphene was used as the bottom electrode contacted with the VP flake to reduce the contact's Schottky barriers.[64] Notably, there are no overlapped regions between the top and bottom Gr layers to avoid the leakage current induced by direct tunneling between two Gr layers. Finally, two Cr/Au electrodes were deposited onto the top and bottom graphene as the source and drain, respectively. The OM image of the MIS tunneling diode is shown in **Figure S4**. This kind of MIS structure allows the manipulation of the tunneling carriers' density by external illumination. Figure 3a shows the I_d-V_d curve of the MIS tunneling diode at V_g = 0 V; the device exhibits an apparent unsymmetric rectifying behaviour with a threshold voltage (V_{th}) in the forward bias. The rectification ratio was calculated at room temperature as ~6.5×10^2 (V_d = ±5 V). The drain current increased exponentially before saturation at a higher V_d as the forward bias was applied beyond the V_{th} ~3.3 V. The whole resistance of the MIS tunneling diode can be divided into two components, *i.e.* the channel resistance and tunneling resistance. Due to the electron blocking of the *h*-BN layer, the

tunneling probability is quite limited when V_d is applied below V_{th}. In contrast, the in-plane channel resistance dominates the whole transport behavior in a higher bias. Figure 3b illustrates the corresponding band diagrams of the MIS tunneling diodes according to the predicted energy band alignment. Theoretically, the work function of monolayer graphene is regarded as ~-4.5 eV below the vacuum level.[65] As for the VP layer, the band structure was extracted from theoretical data of bulk VP, *i.e.* the position of conduction band minima (CBM) was estimated to be ~-4.11 eV below vacuum with the bandgap of ~1.68 eV.[66, 67] According to the energy band alignment, *h*-BN is an electron-blocking layer. When V_d is smaller than V_{th} (panel I, Figure 3b), electrons can seldom transmit into the graphene layer due to the intermediate *h*-BN, consistent with the observed ultralow drain current. As the drain voltage increases gradually over V_{th}, the energy bands of VP bend downward at the interface, resulting in the accumulation of electrons, as shown in panel II of Figure 3b. Electrons are accelerated by the high electrical field and tunnel through the trigonal barriers. The kinetic energy of the electrons translates into hot carriers in graphene, resulting in the exponential increase of the drain current. Back gate voltage can induce electrostatic doping in the 2D channel.[68] The positive potential of V_g makes the Femi level of VP closer to the conduction band (panel III, Figure 3b). More electrons accumulate at the interfaces and tunnel through the blocking layer, resulting in a higher drain current. Figure 3c plots the relationship of tunneling current corresponding to the V_g and V_d. The data was collected from another device without external photo illumination. The saturation current increases as the V_g increases, implying that the in-plane resistance of the VP flake dominates the drain current at high bias. By contrast, the exponential increase of low-bias drain current is independent of V_g, further confirming the low tunneling conduction in the MIS tunneling diode. In addition, the threshold voltage shifted slightly toward the negative direction when the V_g was applied. The V_{th} changed slightly from ~5.5 V

(V_g=0 V) to ~5 V (V_g = 10 V), then almost maintained at ~5 V, further supporting the electron tunneling through the *h*-BN layer. The back gate can store optically generated carriers, which modulates tunneling conduction.[15] In consequence, the vertical MIS tunneling diode was illuminated by a xenon lamp. The large V_d separates the photogenerated electron-hole pairs and then tunnels through the *h*-BN barrier layer. As depicted in Figure 3d, the drain current increased dramatically by ~4.2 times at V_d = 7 V, V_g = 30 V compared with that in the dark. The apparent increase of saturation current further demonstrates that the photo-induced carriers reduced the in-plane resistance of VP channel. Notably, the V_{th} is almost maintained under illumination and the I_d (when$V_d < V_{th}$) is still maintained at a low level, suggesting that the kinetic energy of photo-induced carriers is limited at low-bias voltages. The *h*-BN barrier can efficiently hinder the electron transport between layers and keep the off-state current low, which results in an abrupt increase of the rectification ratio. Once illuminated, the rectification ratio has increased by ~3 times, leading to a great potential application in multifunctioinal optoelectronic devices.

Although exotic characteristics are obtained in the VP-based MIS tunneling diode, the broad applications of the MIS tunneling diode in the high-power fields are still subjected to the small on-state current. Moreover, the considerable sheet resistance also harms heat dissipation in high-density integrated circuits.[11, 69] Therefore, it is essential to moderate the tunneling current to drive high-power devices. The *pn* junction tunneling device is operated by the interband tunneling (IBT) mechanism, which can reach considerable current densities.[4] The energy bands bend steeply in the junction tunneling device due to the degenerated *p/n*-type semiconductors, leading to direct tunneling between the valence and conductive bands. Given the intrinsic *n*-type characteristic of the as-prepared VP, a *p*-type doped VP is required to fabricate the VP-based junction tunneling device.

Consequently, according to the previous report, a mild Ar^+ plasma post-treatment was utilized to control the doping states of the VP fakes.[28] With the Ar^+ plasma-induced surface defects, more H_2O/O_2 molecules were absorbed on the surface to form abundant phosphorus-oxidized species, which results in the extension of the underneath electron depletion layer.[70] Hence, the electron depletion layer became increasingly thicker along with decreased VP thickness (**Figure S5**) in the plasma treatment process, primarily leading to progressive *p*-type doping. Other factors in plasma treatment may also contribute to *p*-type doping, like the reduction of stannous Sn-I-P impurities, which have been described in our previous work.[28] **Figure 4**a shows the transfer curves of an as-fabricated VP FET corresponding to the post-treatment time. As the post-treatment increases, the *p*-branch of the transfer curve appears gradually, confirming the plasma etching-induced *p*-type doping. As the thickness was reduced to only 4.9 nm after 745 s Ar^+ plasma processing, the channel of the VP FET was almost electron-depleted as the thickness decreased. At the same time, the source and drain ends were maintained *n*-type due to the coverage of metal electrodes. Until the end, a VP-based three-terminal TFET with the channel made from the *n*-*p*-*n* junction was fabricated, as demonstrated in the inset of Figure 4a. In addition, the Raman evolution of the VP channel as a function of the Ar^+ plasma exposure time is illustrated in **Figure S6** to verify the crystal quality in the processes. The results demonstrate that the quality of the VP flakes was maintained well through proper therapy using Ar^+ plasma treatment.

Figure 4b shows the abnormal transfer curve (yellow solid line) of the VP-based TFET, which differs from the others with an obvious hump-like I_d-V_g curve due to the interband tunneling between regions.[16] Moreover, the hump is strongly dependent on V_d. When V_d was larger than 1 V, the drain current hump can be observed clearly. And the hump peak voltage shifted toward a larger V_g as the V_d increased, as guided by the black dashed arrow. To further understand the

tunneling process, four representative states (I - IV) are defined to explain the transition of the energy bands under different V_g and V_d. When V_g is much lower than -32 V, the strong negative V_g introduces robust electrostatic *p*-type doping to the VP-based TFET. Simultaneously, taking account of the plasma etching induced *p*-type doping to the channel component, the entire energy bands of the TFET bend upward seriously, as shown in panel I of Figure 4c. Therefore, the hole branch dominates the transfer curve when V_g is much lower than the valley voltage. As the V_g sweeps forward, the electrostatic *p*-type doping is weakened, and the corresponding energy levels bend downward gradually, especially for the source and drain ends. Without electrode protection, the channel part remains *p*-type doped with the energy levels bending upwards, as shown in panel II. As the V_g keeps increasing over the valley voltage, the energy bands near the ends bend downwards more seriously, resulting in an overlap of the energy bands between the *n*-type source/drain and *p*-type channel. Due to the steep bending of energy bands near the junction, there are many occupied states in the conduction bands and unoccupied states in the valence band, as shown in panel III. A large number of electrons can tunnel through the band gaps directly from the VBM to CBM at the *p/n* junctions and give rise to an extreme increase in total current. Hence, the obtained maximum peak/valley current is ~ 40.7/2.0 pA, and the peak/valley voltage is ~ 42/-30 V under V_d= 2.5 V. The huge peak-valley current ratio (PVCR) is much larger than that of most competitors. Specific details about the peak/valley current are given in **Figure S7** and **Table S1**. Subsequently, as the V_g keeps sweeping forward over the peak voltage, *i.e.,* 33 V, holes in the *p*-type channel are depleted more and more seriously, resulting in the disappearance of the overlap between CBM and VBM in the *n*- and *p*-regions. Therefore, the tunneling component in the total drain current decreases with the dominating drift component, and the abnormal transfer behavior of negative differential transconductance (NDT) is obtained, as shown in the state IV in Figure 4b,

c. Furthermore, as the V_g increased more positively, an inversion layer may appear in the channel part. Then, the tunneling current no longer affects the operation of the NDT FET, and the electron carriers can drift directly from the source to the drain by shrinking the Schottky barriers at the electrodes. Notably, limited to the SiO_2 dielectric layer (~285 nm), the V_g cannot be oversupplied in our experiments. To sum up, due to the interband tunneling, the NDT effect is ascribed to the accumulation of opposite charge carriers at the interface between the channel and drain. More importantly, the bias voltage V_d can also influence the NDT effect ascribing to the alignment of quasi-Fermi levels in different regions. Specifically, a larger V_d leads to a wider misalignment of the quasi-Fermi levels in the reversed channel/drain junction. In that case, V_g can more effectively modulate the channel's conductance. The transconductance of TFET ($g_m = dI_D/dV_g$) is defined to reflect the sensitivity of drain current to the input voltage, *i.e.,* V_g. Figure 4d demonstrates the relationship between g_m and V_g under different V_d. As the g_m is extracted from I_d-V_g curves, both positive and negative transconductance regions can be observed. With the increase of V_d, the maximum of g_m at V_d=2.7 V reaches 0.97 pS, suggesting the enhancement of the gate tunability. However, the onset for NDT regions corresponding to different V_d gradually shifts positively, implying a larger V_d makes it harder to realize multivalues.[71] Therefore, another effective method is needed urgently to trade off the V_d and V_g. Taking account of the extraordinary photoelectrical properties of VP flakes, visible light illumination has been used to modulate the NDT effect. Figure 4e compares the performance of the NDT FET under illumination against the dark. Herein, V_d was set to be 1.5 V in both cases. The maximum of g_m under illumination (~0.361 pS) has increased by 2 times compared with the dark one (~0.174 pS). Meanwhile, the NDT region's onset has also shifted negatively from 37 V (dark) to 32 V (illumination). When the VP-based TFET is illuminated, electrons can obtain excess energy to get excited towards the conductive band (CB)

of VP, which increases the minor carrier electrons in the *p*-type channel part. Then, the excess electrons in the CB can drift from channel to drain and lead to a larger g_m at the same V_g. The value of V_g is responsible for the degree of band bending, which greatly influences the band alignment. As the electron population in the drain region increases dramatically, the quasi-Fermi level shifts upward, as depicted in the inset of Figure 4e, which brings forward the interband tunneling window. Hence, the NDT region under illumination starts at a smaller V_g under the same V_d. Further investigation of the NDT effect corresponding to the incident wavelength was carried out by inserting monochromatic filters with different wavelengths into the incident light. As the bandgap of VP flake ranges from 1.68 to 2.02 eV with the thickness down from bulk to monolayer[67, 72], thinner VP flakes require more energy to excite photogenerated carriers. **Figure S8** depicts the g_m-V_g curves excited by the light with different wavelengths. As the photon energy increases, the maximum of g_m increases correspondingly because more electrons were excited to the CB of the VP flakes by photons with higher energy. Simultaneously, the onset for the NDT region gradually shifted toward a smaller V_g due to the above-mentioned upward bending of the quasi-Fermi level in the drain region. Therefore, illuminating the TFET enhances the tunning ability of gate bias and allows the NDT effect to be realized more readily in the same conditions of gate and drain biases. Illumination supplies an effective terminal for the NDT modulation.

3. Conclusions

In conclusion, we have comprehensively investigated the electron transport properties of various VP-based tunneling structures. In detail, the underlying mechanism of the VP-based MIS tunneling diodes has been demonstrated to have excellent performance compared to conventional *p-n* diodes, such as the high rectification ratio. Moreover, a pronounced NDT effect is observed in the lateral

n-p-n homojunction tunneling FET due to the carriers' interband tunneling. Interestingly, those behaviors can be tuned continuously by bias conditions and ordinary light illumination instead of high-power lasers, which boosts the development of 2D tunneling devices with multiple controlling strategies. Finally, the sign-switching transconductance observed in our VP-based tunneling devices has immense potential for designing future energy-efficient and multifunctional devices at the 2D limit.

4. Experimental Section

Crystal growth: Bulk VP crystal was grown by the chemical vapor transport (CVT) method with the precursors of amorphous red phosphorus (400 mg, ≥ 97 %), granular iodine (25 mg, 99.8 %), and tin (35 mg, 99.995 %). The precursors were sealed into an evacuated ampoule and heated by a tube furnace. More detailed CVT growth conditions can be found in our previous work.[28]

Device fabrication: Exfoliated few-layer VP flakes were deposited onto 285 nm SiO2 /Si^{++} substrate as the channel for the phototransistor. Standard e-beam lithography was employed to define the source and drain electrodes. Subsequently, Cr/Au (5/50 nm) was deposited by e-beam evaporation as the metal electrodes. For the metal-insulator-semiconductor tunnelling diode, graphene was first mechanically exfoliated onto the substrate as the bottom electrode for the metal-insulator-semiconductor tunneling diode. Then, a few-layer VP flake was transferred onto the bottom graphene by the dry-transfer method with partial contact with the bottom Gr. Subsequently, a piece of *h*-BN flake with a thickness of ~ 5 nm was transferred to cover the whole VP flake as the insulator. Finally, the top graphene electrode was transferred by the same method to the topmost with a partial VP channel covered in case of the direct tunneling between the two graphene electrodes. For the *n-p-n* homojunction tunneling field-effect transistor, a mild Ar^{+} plasma etching

process was employed to deal with the as-fabricated VP-based FET with standard back-gated geometry. As the plasma processes continued, the channel of the FET became thinner and had more defects on the surface. After 745 s treatment, the thickness of the channel was reduced to ~4.9 nm, while the source and drain regions were almost maintained due to the coverage of the metal electrodes. Hence, the TFET was fabricated with a variation in thickness from source to drain. This process was conducted on a TRION ICP-RIE system with 30 sccm argon flow at 10 mTorr pressure. The ICP and RIE power was set to 250 and 40 W, respectively.

Characterization: Raman and PL spectra were implemented on a WITec alpha 300R confocal micro-Raman system excited by a 532 nm continuous-wave laser. The laser power was no larger than 0.5 mW in case the VP flakes were degraded. The structural properties of the VP flake were characterized by a JEOL JEM-2100F STEM and energy dispersive X-ray (EDX) operated at 200 kV.

Electrical and photoelectrical measurement: All the electrical measurements were carried out at room temperature using a Lakeshore probe station with a Keithley 4200 semiconductor parameter analyzer. The illuminated output and transfer characteristics were compared with the dark ones throughout the work using a 300 W xenon lamp. Laser diodes are the illumination sources that excite the power-dependent and time-dependent photocurrents.

Supporting Information

Supporting Information is available from the Wiley Online Library or from the author.

Acknowledgements

This work is financially supported by the Hong Kong Polytechnic University grant (1-YY5U) and the Research Grants Council of Hong Kong (Project nos. 15306321 and 15307423). Y. Y. L acknowledgements the support of the National Natural Science Foundation of China (No.12204152) and the Yellow River Scholar Start-up Foundation of Henan University.

Conflict of Interest

The authors declare no conflict of interest.

Data Availability Statement

The data that support the findings of this study are available from the corresponding author upon reasonable request.

References

[1] A. M. Ionescu, H. Riel, *Nature* **2011**, *479*, 329-337.

[2] H. Ilatikhameneh, Y. Tan, B. Novakovic, G. Klimeck, R. Rahman, J. Appenzeller, *IEEE Journal on Exploratory Solid-State Computational Devices and Circuits* **2015**, *1*, 12-18.

[3] K. R. Kim, D. H. Kim, K. W. Song, G. Baek, H. H. Kim, J. I. Huh, J. D. Lee, B. G. Park, *IEEE Electron Device Lett.* **2004**, *25*, 439-441.

[4] L. Esaki, *IEEE Transctions on Electron Devices* **1976**, *23*, 644-647.

[5] J. H. Lim, J. Shim, B. S. Kang, G. Shin, H. Kim, M. Andreev, K. S. Jung, K. H. Kim, J. W. Choi, Y. Lee, J. H. Park, *Adv. Funct. Mater.* **2019**, *29*, 19055410.

[6] C. Kim, Y. Lee, S. Lee, *J. Appl. Phys.* **2017**, *121*, 124504.

[7] A. Nourbakhsh, A. Zubair, M. S. Dresselhaus, T. Palacios, *Nano Lett.* **2016**, *16*, 1359-1366.

[8] I. Gayduchenko, S. G. Xu, G. Alymov, M. Moskotin, I. Tretyakov, T. Taniguchi, K. Watanabe, G. Goltsman, A. K. Geim, G. Fedorov, D. Svintsov, D. A. Bandurin, *Nat. Commun.* **2021**, *12*, 543.

[9] B. Romeira, J. M. L. Figueiredo, C. N. Ironside, A. E. Kelly, T. J. Slight, *IEEE Photonic. Tech. Lett.* **2010**, *22*, 1610-1612.

[10] S. Lee, Y. Lee, C. Kim, *Sci. Rep.* **2017**, *7*, 11065.

[11] J. W. Lee, W. Y. Choi, *Solid State Electron.* **2020**, *163*, 107659.

[12] S. Fan, Q. A. Vu, S. Lee, T. L. Phan, G. Han, Y. M. Kim, W. J. Yu, Y. H. Lee, *ACS Nano* **2019**, *13*, 8193-8201.

[13] Y. W. Lan, C. M. Torres, S. H. Tsai, X. Zhu, Y. Shi, M. Y. Li, L. J. Li, W. K. Yeh, K. L. Wang, *Small* **2016**, *12*, 5676-5683.

[14] M. Zubair, H. Wang, Q. Zhao, M. Kang, M. Xia, M. Luo, Y. Dong, S. Duan, F. Dai, W. Wei, Y. Li, J. Wang, T. Li, Y. Fang, Y. Liu, R. Xie, X. Fu, L. Dong, J. Miao, *Small* **2023**, *19*, 2300010.

[15] J. Shim, S.-H. Jo, M. Kim, Y. J. Song, J. Kim, J.-H. Park, *ACS Nano* **2017**, *11*, 6319-6327.

[16] W. Uddin, V. Dhyani, G. Ahmad, V. Kumar, P. K. Muduli, S. Das, *ACS Appl. Electron. Mater.* **2020**, *2*, 1567-1573.

[17] Y. Wang, L. Mei, Y. Li, X. Xia, N. Cui, G. Long, W. Yu, W. Chen, H. Mu, S. Lin, *Phys. Rep.* **2024**, *1081*, 1-46.

[18] W. Ahmad, A. Abbas, U. Younis, J. Zhang, S. H. Aleithan, Z. Wang, *Adv. Funct. Mater.* **2024**, *DOI: 10.1002/adfm.202410723*, 2410723.

[19] X. Liu, S. Wang, Z. Di, H. Wu, C. Liu, P. Zhou, *Adv. Sci.* **2023**, *10*, 2301851.

[20] J. Xue, S. Wang, J. Zhou, Q. Li, Z. Zhou, Q. Hui, Y. Hu, Z. Zhou, Z. Feng, Q. Yan, Y. Yu, Y. Weng, R. Tang, X. Su, Y. Xin, F. Zheng, S. Ju, L. You, L. Fang, *Appl. Phys. Lett.* **2023**, *122*, 181903.

[21] R. Cheng, L. Yin, R. Hu, H. Liu, Y. Wen, C. Liu, J. He, *Adv. Mater.* **2021**, *33*, 2008329.

[22] Y. L. Lu, S. Dong, W. Zhou, S. Dai, B. Zhou, H. Zhao, P. Wu, *Phys. Chem. Chem. Phys.* **2018**, *20*, 11967-11975.

[23] G. Fasol, M. Cardona, W. Honle, H. G. v. Schnering, *Solid State Commun.* **1984**, *52*, 307-310.

[24] C. G. Michel, R. Schachter, M. A. Kuck, J. A. Baumann, P. M. Raccah (Stauffer Chemical Company), *US. 4,620,968*, **1986**.

[25] G. Schusteritsch, M. Uhrin, C. J. Pickard, *Nano Lett.* **2016**, *16*, 2975-2980.

[26] H. Thurn, H. Krebs, *Angew. Chem. Int. Ed.* **1966**, *12*, 1047-1048.

[27] M.A. Kuck, J.A. Baumann, C. G. Michel, S. W. Gersten, *J. Cryst. Growth* **1984**, *68*, 644-646.

[28] Y. Li, S. Cai, W. K. Lai, C. Wang, L. Rogée, L. Zhuang, L. Zhai, S. Lin, M. Li, S. P. Lau, *Adv. Opt. Mater.* **2022**, *10*, 2101538.

[29] Y. Y. Li, Z. X. Hu, S. H. Lin, S. K. Lai, W. Ji, S. P. Lau, *Adv. Funct. Mater.* **2017**, *27*, 1600986.

[30] P. H. Tan, W. P. Han, W. J. Zhao, Z. H. Wu, K. Chang, H. Wang, Y. F. Wang, N. Bonini, N. Marzari, N. Pugno, G. Savini, A. Lombardo, A. C. Ferrari, *Nat. Mater.* **2012**, *11*, 294-300.

[31] C. Lee, H. Yan, L. E. Brus, T. F. Heinz, J. Hone, S. Ryu, *ACS Nano* **2010**, *4*, 2695.

[32] A. G. Ricciardulli, Y. Wang, S. Yang, P. Samori, *J. Am. Chem. Soc.* **2022**, *144*, 3660-3666.

[33] Z. Sun, Z. Cai, P. Cheng, L. Chen, X. Zhao, J. Zhang, K. Wu, B. Feng, *NPJ 2D Mater. Appl.* **2023**, *7*, 37.

[34] L. Zhang, H. Huang, Z. Lv, L. Li, M. Gu, X. Zhao, B. Zhang, Y. Cheng, J. Zhang, *ACS Appl. Electron. Mater.* **2021**, *3*, 1043-1049.

[35] W. Chen, A. Chen, R. Zhang, J. Zeng, L. Zhang, M. Gu, C. Wang, M. Huang, Y. Guo, H. Duan, C. Hu, W. Shen, B. Niu, K. Watanabe, T. Taniguchi, J. Zhang, J. Li, X. Cai, G. Liu, *Nano Lett.* **2023**, *23*, 10821-10831.

[36] D. J. Olego, J. A. Baumann, M. A. Kuck, R. Schachter, C. G. Michel, *Solid State Commun.* **1984**, *52*, 311-314.

[37] G. Zhang, A. Chaves, S. Huang, F. Wang, Q. Xing, T. Low, H. Yan, *Sci. Adv.* **2018**, *4*, eaap9977.

[38] H. Song, H. Mu, J. Yuan, B. Liu, G. Bai, S. Lin, *SusMat* **2023**, *3*, 543-554.

[39] H. Chen, W. Fei, J. Zhou, C. Miao, W. Guo, *Small* **2017**, *13*, 1602336.

[40] C. Ruppert, O. B. Aslan, T. F. Heinz, *Nano Lett.* **2014**, *14*, 6231-6.

[41] Y. Lin, X. Ling, L. Yu, S. Huang, A. L. Hsu, Y.-H. Lee, J. Kong, M. S. Dresselhaus, T. Palacios, *Nano Lett.* **2014**, *14*, 5569-5576.

[42] J. S. Ross, S. Wu, H. Yu, N. J. Ghimire, A. M. Jones, G. Aivazian, J. Yan, D. G. Mandrus, D. Xiao, W. Yao, X. Xu, *Nat. Commun.* **2013**, *4*, 1474.

[43] F. Xia, T. Mueller, Y. M. Lin, A. Valdes-Garcia, P. Avouris, *Nat. Nanotechnol.* **2009**, *4*, 839-843.

[44] M. Buscema, D. J. Groenendijk, S. I. Blanter, G. A. Steele, H. S. J. van der Zant, A. Castellanos-Gomez, *Nano Lett.* **2014**, *14*, 3347-3352.

[45] M.-L. Lu, T.-M. Weng, J.-Y. Chen, Y.-F. Chen, *NPG Asia Mater.* **2012**, *4*, e26-e26.

[46] Q. Zhao, W. Wang, F. Carrascoso-Plana, W. Jie, T. Wang, A. Castellanos-Gomez, R. Frisenda, *Mater. Horizons* **2020**, *7*, 252-262.

[47] W. Zhang, C. P. Chuu, J. K. Huang, C. H. Chen, M. L. Tsai, Y. H. Chang, C. T. Liang, Y. Z. Chen, Y. L. Chueh, J. H. He, M. Y. Chou, L. J. Li, *Sci. Rep.* **2014**, *4*, 3826.

[48] G. Konstantatos, M. Badioli, L. Gaudreau, J. Osmond, M. Bernechea, F. P. Garcia de Arquer, F. Gatti, F. H. Koppens, *Nat. Nanotechnol.* **2012**, *7*, 363-8.

[49] A. Castellanos-Gomez, L. Vicarelli, E. Prada, J. O. Island, K. L. Narasimha Acharya, S. I. Blanter, D. J. Groenendijk, M. Buscema, G. A. Steele, J. V. Alvarez, H. W. Zandbergen, J. J. Palacios, H. S. J. van der Zant, *2D Mater.* **2014**, *1*, 025001.

[50] M. Ruck, D. Hoppe, B. Wahl, P. Simon, Y. Wang, G. Seifert, *Angew. Chem. Int. Ed.* **2005**, *44*, 7616-9.

[51] C. Soci, A. Zhang, B. Xiang, S. A. Dayeh, D. P. R. Aplin, J. Park, X. Y. Bao, Y. H. Lo, D. Wang, *Nano Lett.* **2007**, *7*, 1003-1009.

[52] B. Radisavljevic, A. Radenovic, J. Brivio, V. Giacometti, A. Kis, *Nat. Nanotechnol.* **2011**, *6*, 147-50.

[53] L. Li, Y. Yu, G. J. Ye, Q. Ge, X. Ou, H. Wu, D. Feng, X. H. Chen, Y. Zhang, *Nat. Nanotechnol.* **2014**, *9*, 372-377.

[54] J. Knoch, M. Zhang, J. Appenzeller, S. Mantl, *Appl. Phys. A* **2007**, *87*, 351-357.

[55] S. Das, H. Y. Chen, A. V. Penumatcha, J. Appenzeller, *Nano Lett.* **2013**, *13*, 100-105.

[56] W. Chen, R. Zhang, M. Gu, L. Zhang, B. Xie, Z. Yu, A. Chen, J. Li, S. Liu, P. Gao, J. Zhang, X. Cai, G. Liu, *Adv. Opt. Mater.* **2023**, *12*, 2301399.

[57] S. Ghosh, A. Varghese, K. Thakar, S. Dhara, S. Lodha, *Nat. Commun.* **2021**, *12*, 3336.

[58] B. Liu, A. Abbas, C. Zhou, *Advanced Electronic Materials* **2017**, *3*, 1700045.

[59] Changyong Lan, Chun Li, Yi Yin, Huayang Guo, S. Wang, *J. Mater. Chem. C* **2015**, *3*, 8074-8079.

[60] L. Zeng, L. Tao, C. Tang, B. Zhou, H. Long, Y. Chai, S. P. Lau, Y. H. Tsang, *Sci. Rep.* **2016**, *6*, 20343.

[61] N. Dagtekin, A. M. Ionescu, *Appl. Phys. Lett.* **2014**, *105*, 232105.

[62] G. Nazir, A. Rehman, S.-J. Park, *ACS Appl. Mater. Interfaces* **2020**, *12*, 47127-47163.

[63] M. Huang, S. Li, Z. Zhang, X. Xiong, X. Li, Y. Wu, *Nat. Nanotechnol.* **2017**, *12*, 1148-1154.

[64] B. Wei, Y. Li, T. Yun, Y. Li, T. Gui, W. Yu, H. Mu, N. Cui, W. Chen, S. Lin, *Mater. Futures* **2024**, *3*, 025302.

[65] S. M. Song, J. K. Park, O. J. Sul, B. J. Cho, *Nano Lett.* **2012**, *12*, 3887-92.

[66] Y. Xu, Q. Long, D. Li, P. Li, *Phys. Chem. Chem. Phys.* **2022**, *24*, 3379-3385.

[67] B. Zhang, Z. Wang, H. Huang, L. Zhang, M. Gu, Y. Cheng, K. Wu, J. Zhou, J. Zhang, *J. Mater. Chem. A* **2020**, *8*, 8586-8592.

[68] H. Liu, A. T. Neal, P. D. Ye, *ACS Nano* **2012**, *6*, 8563-8569.

[69] W. Cao, J. Jiang, J. Kang, D. Sarkar, W. Liu, K. Banerjee In *Designing band-to-band tunneling field-effect transistors with 2D semiconductors for next-generation low-power VLSI*, 2015 IEEE International Electron Devices Meeting (IEDM), 7-9 Dec. 2015; 2015; pp 12.3.1-12.3.4.

[70] H. Nan, Z. Wang, W. Wang, Z. Liang, Y. Lu, Q. Chen, D. He, P. Tan, Feng Miao, X. Wang, J. Wang, Z. Ni, *ACS Nano* **2014**, *8*, 5738-5745.

[71] T. Li, X. Li, M. Tian, Q. Hu, X. Wang, S. Li, Y. Wu, *Nanoscale* **2019**, *11*, 4701-4706.

[72] R. Zhao, X. Zhao, X. Xu, Y. Zhang, Y. Wang, M. Jin, Z. Liu, Y. Cheng, H. Zheng, J. Zhang, *J Phys Chem Lett* **2022**, *13*, 8236-8244.

Figures & Captions

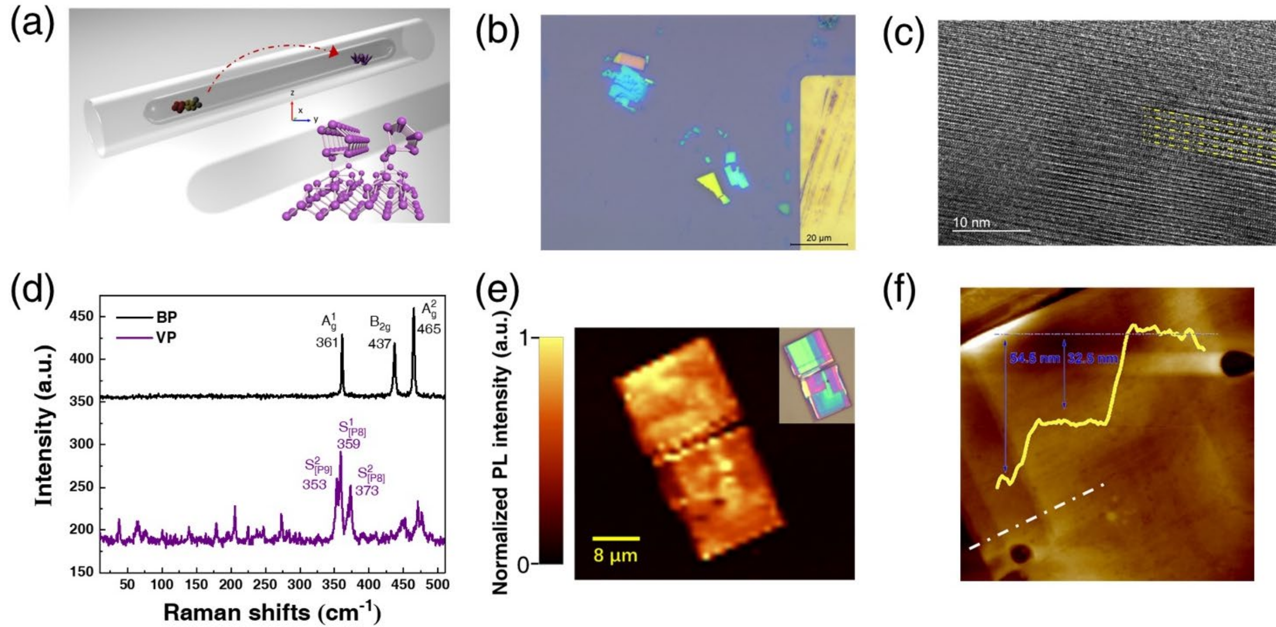

Figure 1. Atomic structure of the VP crystal and characterization. a) Schematic illustration of the synthesis process of VP crystals *via* CVT method in RP/Sn/I_2 reaction system. The inset depicts the atomic structure of VP crystals, clearly exhibiting the linked perpendicular tubular structures. b) OM image of mechanically exfoliated few-layer VP flakes on the 285 nm SiO_2/Si^{++} substrate. c) High-resolution TEM image of the VP flake. The yellow parallel dashed lines indicate the orientation of phosphorus tubes. d) Raman spectra of VP and BP, respectively. The three highlighted Raman peaks are stretching modes of P8 and P9 cages, respectively. e) Normalized PL intensity mapping of a VP flake with different thicknesses under 532 nm excitation. The inset is the corresponding OM image. f) AFM image of the corresponding VP flake shown in panel e. Height trace of the flake along the marked white solid line. Clear stages with different heights were measured out along the marked line.

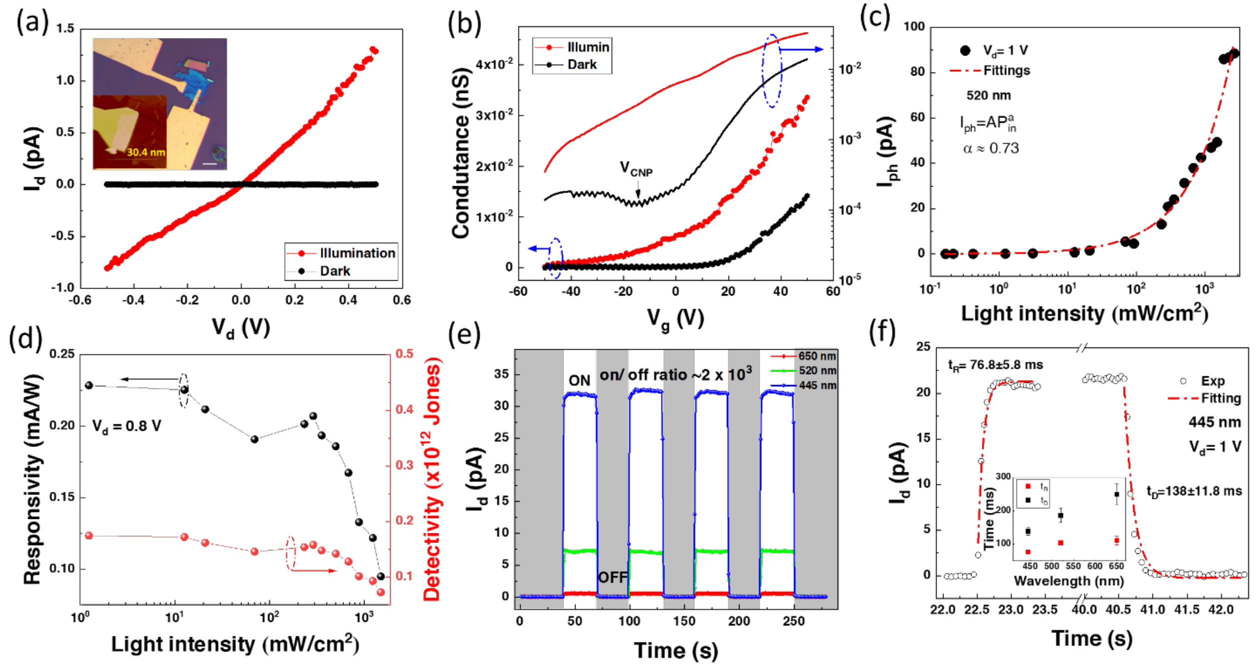

Figure 2. Photoelectronic characteristics of the VP-based phototransistor. a) The output curves *w/* and *w/o* illumination under V_g=0 V, where a xenon lamp was used as the illumination source. The photo of the VP-based phototransistor is given in the inset. The corresponding AFM image illustrates that the thickness of the VP flake is ~30.4 nm. b) Both the linear and logarithmic plots of the transfer curves *w/* and *w/o* illumination under V_d= 0.5 V. Obvious ambipolar feature is found in the dark. c) Photocurrent as a function of the illumination light power density fitted by the power-law. A 520 nm laser diode was used to excite the phototransistor. d) Light intensity-dependent responsivity and specific detectivity of the VP-based phototransistor. The drain bias was set as 0.8 V without applied gate voltage. e) Time-dependent photoresponse excited by a pulsed laser with various wavelengths exhibits a high photocurrent switch on/off ratio. The applied V_d was 0.5 V and the incident laser power density P_{in} was 122.3 mW cm^{-2}. (f) Photoresponse time analysis of the VP phototransistor under a 445 nm laser diode illumination. The applied V_d was 1

V, and the laser power density P_{in} was 0.5 W cm^{-2}. The inset shows the wavelength-dependent photoresponse rise and decay time.

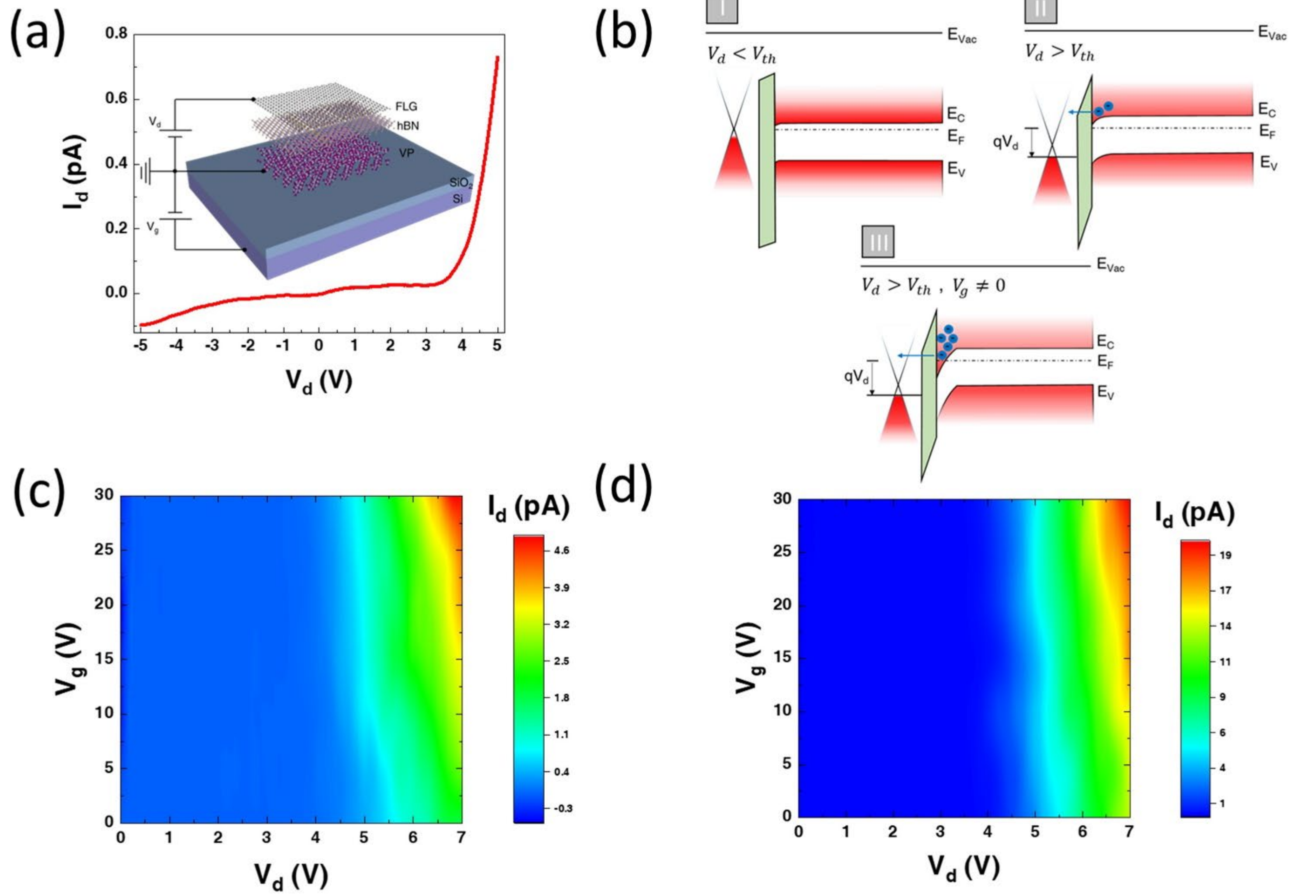

Figure 3. Transport characteristics of VP-based metal/insulator/semiconductor (MIS) tunneling diode. a) I_d-V_d curve of the Gr/*h*-BN/VP vertical MIS tunneling diode at V_g = 0 V. Inset is the schematic view of the MIS tunneling diode made of vdW heterostructures. b) Band alignment of the tunneling diode in different conditions of V_d and V_g. The tunneling current as a function of the applied V_g and V_d without illumination (c) and with external xenon lamp illumination (d), respectively.

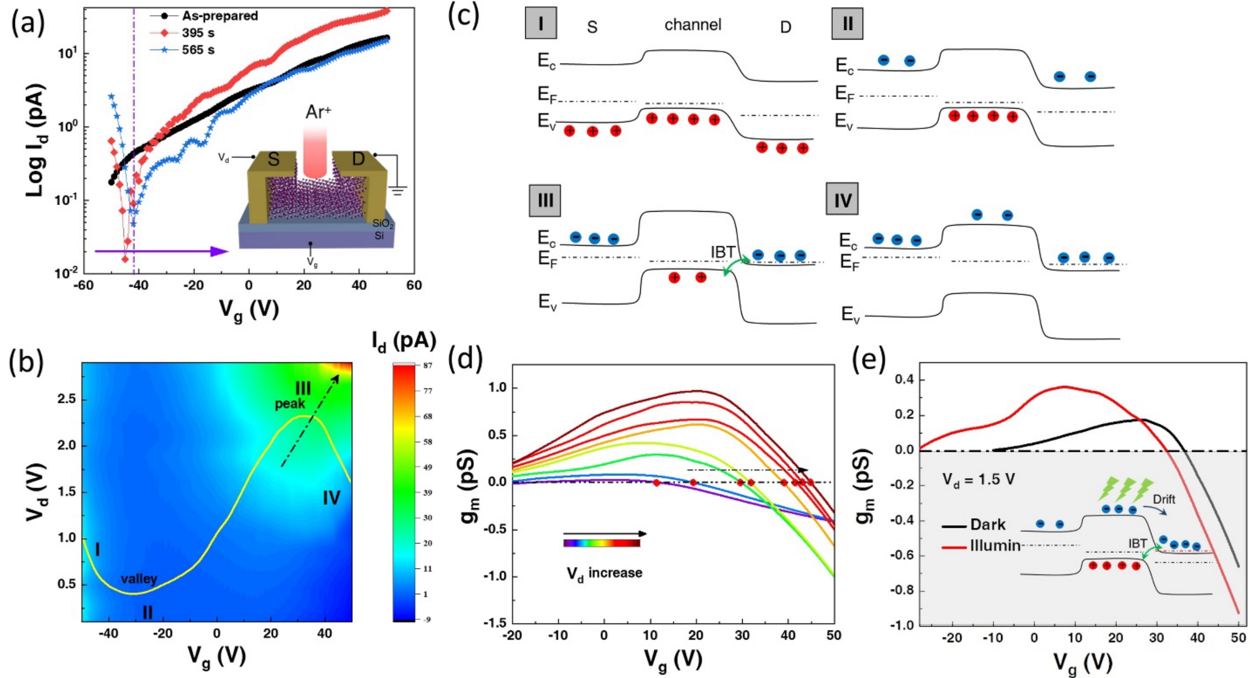

Figure 4. Transport characteristics of the VP-based *n-p-n* homojunction tunneling FET. a) Transfer curves of the VP FET in logarithmic scale as a function of the Ar^{+} plasma exposure time. A clear shift of the V_{CNP} can be observed as the plasma treatment increases. The inset illustrates the schematic diagram of the obtained *n-p-n* homojunction tunneling FET after 745 s treatment. b) 2D plot of the drain current as a function of V_d and V_g. A representative yellow solid line illustrates the transfer curve with V_d=1.9 V. Four representative states are marked with labels from I to IV. c) Schematic band diagrams of the VP-based tunneling FET at corresponding states. d) The sign switching of the transconductance (g_m) as a function of V_g and V_d. As the V_d increases, the onset of the NDT region gradually shifts toward a larger V_g, indicated by the black arrow. e) Comparison of the NDT effect *w/* and *w/o* illumination under V_d=1.5 V. A xenon lamp was used as the light source. The inset shows the corresponding energy band profile of the VP-based tunneling FET under illumination.

Table of Contents

Strong light-matter interaction in violet phosphorus generates photo-induced carriers under visible light illumination. Through investigating the carriers' transport characteristics in VP-based tunneling diodes and tunneling field-effect transistors, light tunability is demonstrated as an efficient method for tunneling modulation, opening new avenues for designing future multifunctional devices at the 2D limit.

Yanyong Li, Haolong Wu, Lyuchao Zhuang, Wai Kin Lai, Shenghuang Lin* and Shu Ping Lau*

Efficient Optical Control of Quantum Tunneling Devices Based on Layered Violet Phosphorus

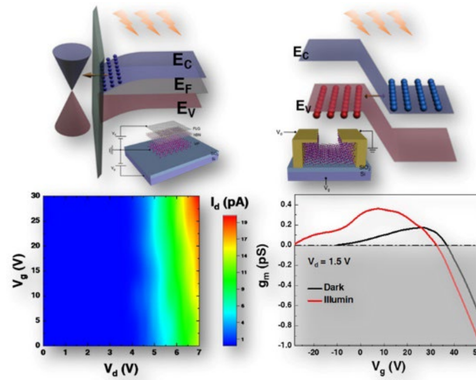

Supporting Information

Efficient Optical Control of Quantum Tunneling Devices Based on Layered Violet Phosphorus

Yanyong Li[1,2], Haolong Wu[1], Lyuchao Zhuang[2], Wai Kin Lai[2], Shenghuang Lin[3,],*

Shu Ping Lau[2,]*

Dr. Y. Y. Li, H. L. Wu, Dr. L. C. Zhuang, W. K. Lai, Prof. S. P. Lau

[1.] Henan Key Laboratory of Quantum Materials and Quantum Energy, School of Quantum Information Future Technology, Henan University, Kaifeng, 475000, Henan, P. R. China

[2.] Department of Applied Physics, The Hong Kong Polytechnic University, Hung Hom, Kowloon, Hong Kong SAR, P. R. China

E-mail: apsplau@polyu.edu.hk

Dr. S. H. Lin

[3.] Songshan Lake Materials Laboratory, Dongguan, 523808, Guangdong, P. R. China

E-mail: linshenghuang@sslab.org.cn

Keywords: violet phosphorus, photoresponse, tunneling diode, tunneling FET, interband tunneling, negative differential transconductance

Contents

S1. Atomic structure of the VP crystal and corresponding repeating units

S2. Characterization of few-layer VP flake by HR-TEM

S3. Photoluminescence of few-layer VP flake

S4. Photo of the VP-based MIS tunneling diode

S5. Channel thickness variation of the VP-based TFET in the process of Ar^+ plasma treatment

S6. Raman spectrum evolution of the VP channel in the process of Ar^+ plasma treatment

S7. The relationship of PVCR as a function of the drain bias in the VP TFET

S8. Wavelength dependent NDT effect

Table S1. Comparison of the PVCR for various tunneling devices based on homojunctions

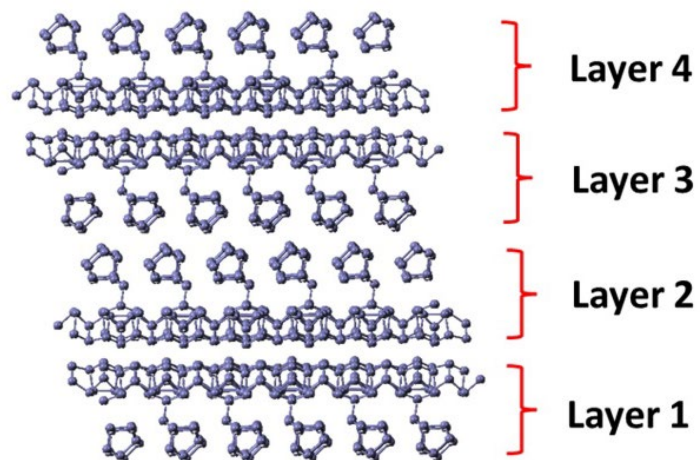

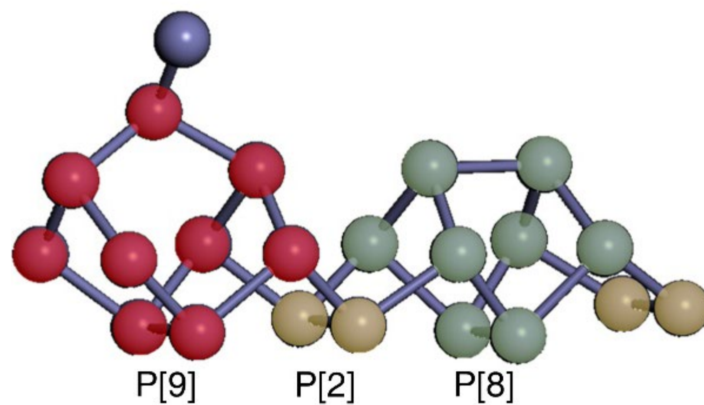

Figure S1. Schematic diagram of the repeating units of VP crystal.

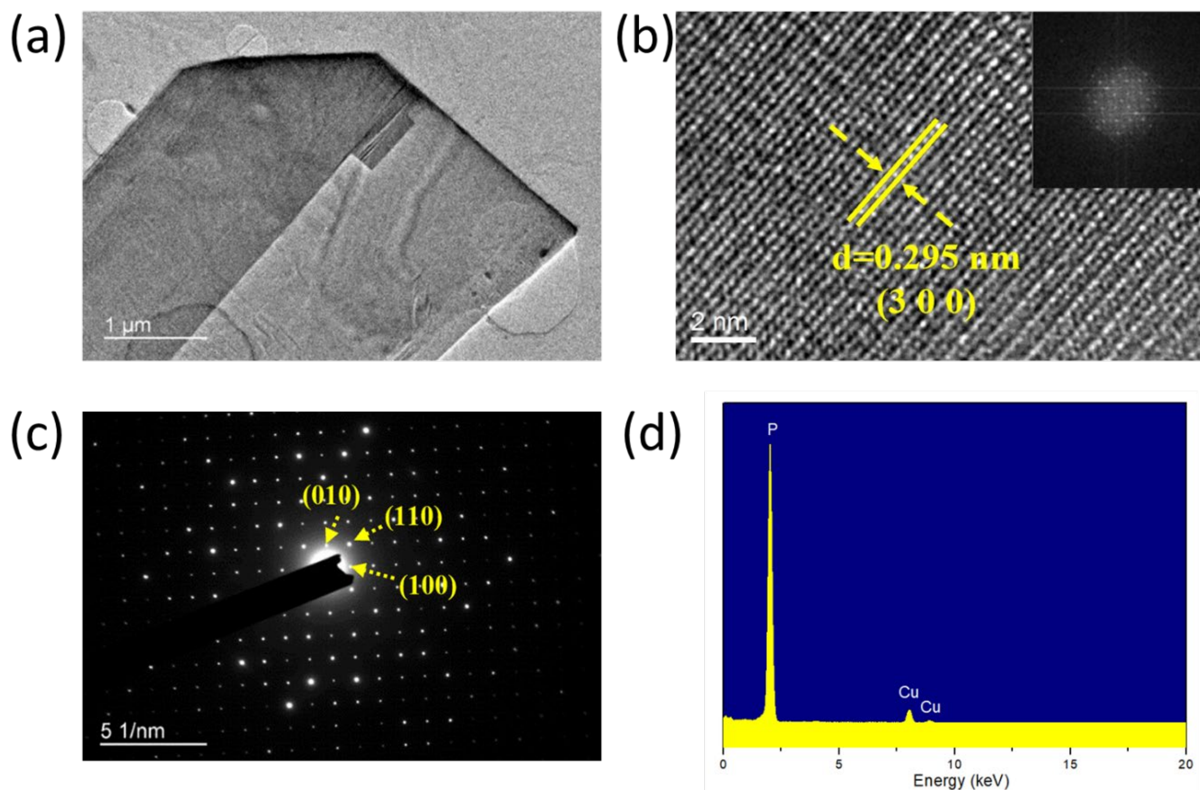

Figure S2. Characterization of VP crystals. a) TEM image of a VP flake. b) HR-TEM image of the corresponding VP flake. The inset gives the FFT transform. c) The selective area electron diffraction (SAED) pattern of the VP flake. (d) The EDS spectrum of the VP flake.

To further characterize the synthesized VP crystals, scanning transmission electron microscopy (STEM) was employed to scrutinize the atomic structure of VP crystals. **Figure S2**a shows the low-magnification STEM imaging of a VP flake with sharp edges on a carbon grid. The obvious STEM imaging contrast demonstrates that regions with different thicknesses exist in one VP flake .[1] High-magnified STEM imaging of the VP flake is given in Figure S2b. Clear lattice fringes reveal the periodic crystalline structure, which is also demonstrated by the fast Fourier transformation (FFT) shown in the inset of Figure S2b. The crystal plane distance between the adjacent lattice fringe was calculated to be ~ 0.295 nm, corresponding to the (3 0 0) crystal plane of the monoclinic crystal structure by ICDD-PDF: NO. 75-577.[2] The sharp and narrow diffraction

spots in the selected area electron diffraction (SAED) pattern (Figure S2c) indicate the high crystalline quality of the VP crystals with three dash arrows assigned to (0 1 0), (1 1 0) and (1 0 0) crystal planes. The *d*-spacings are estimated to be ~ 9.3, 6.6 and 9.1Å, respectively. The VP flake's energy dispersive X-ray spectrum (EDX) was used to confirm its chemical composition, as shown in Figure S2d. The sharp peak of the elemental P is observed at 2.45 keV with only a tiny Cu peak at 7.9 keV from the substrate grid, confirming the VP flake's high purity, consistent with the crystalline nature.

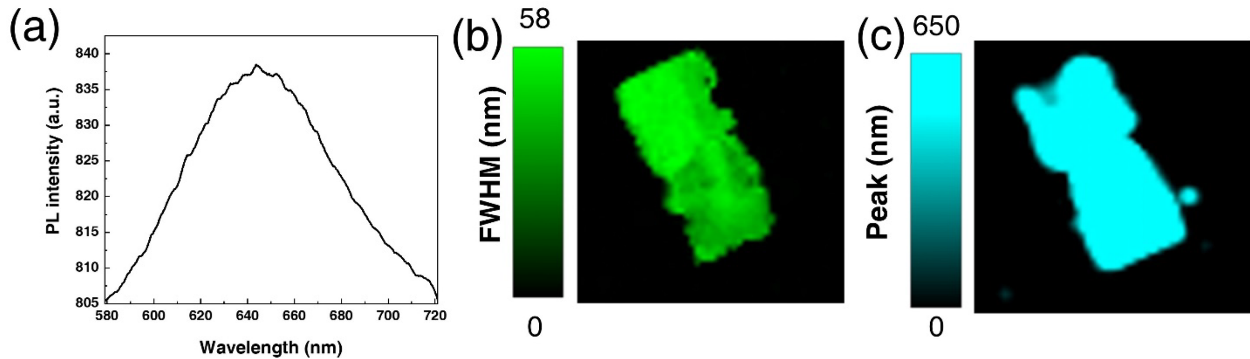

Figure S3. Photoluminescence (PL) of the VP flake. a) Single PL spectrum of the VP flake corresponding to the PL intensity mapping shown in Figure 1e of the main text. The corresponding mapping of PL peak FWHM (b) and peak position (c), respectively.

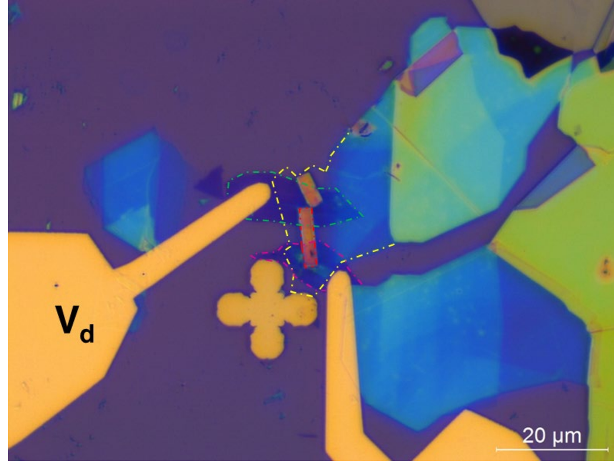

Figure S4. Optical microscope image of the Graphene/*h*-BN/VP MIS tunneling diode. The vertical tunneling diode was fabricated sequentially by dry transfer stacking graphene/*h*-BN/VP. The cerise, yellow, red, and green dash-dot lines correspond to the top Gr, *h*-BN, VP, and bottom Gr, respectively.

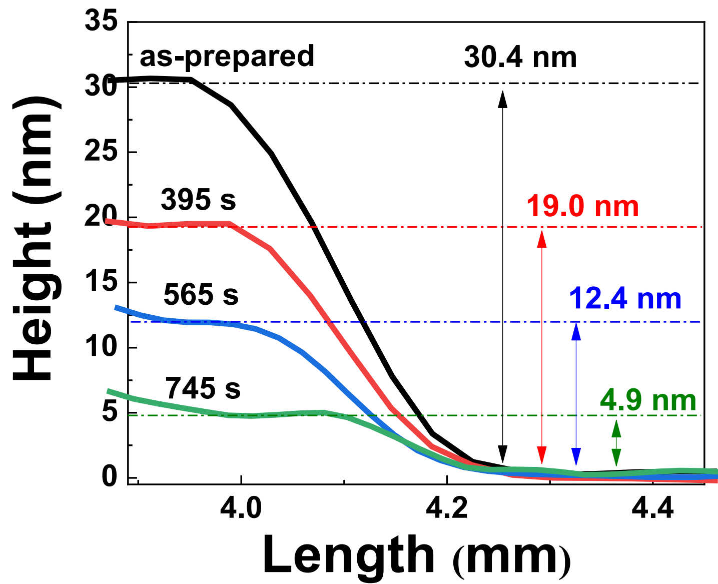

Figure S5. The thickness of the VP channel in the *n*-*p*-*n* homojunction tunneling FET as a function of the Ar^+ plasma processing time.

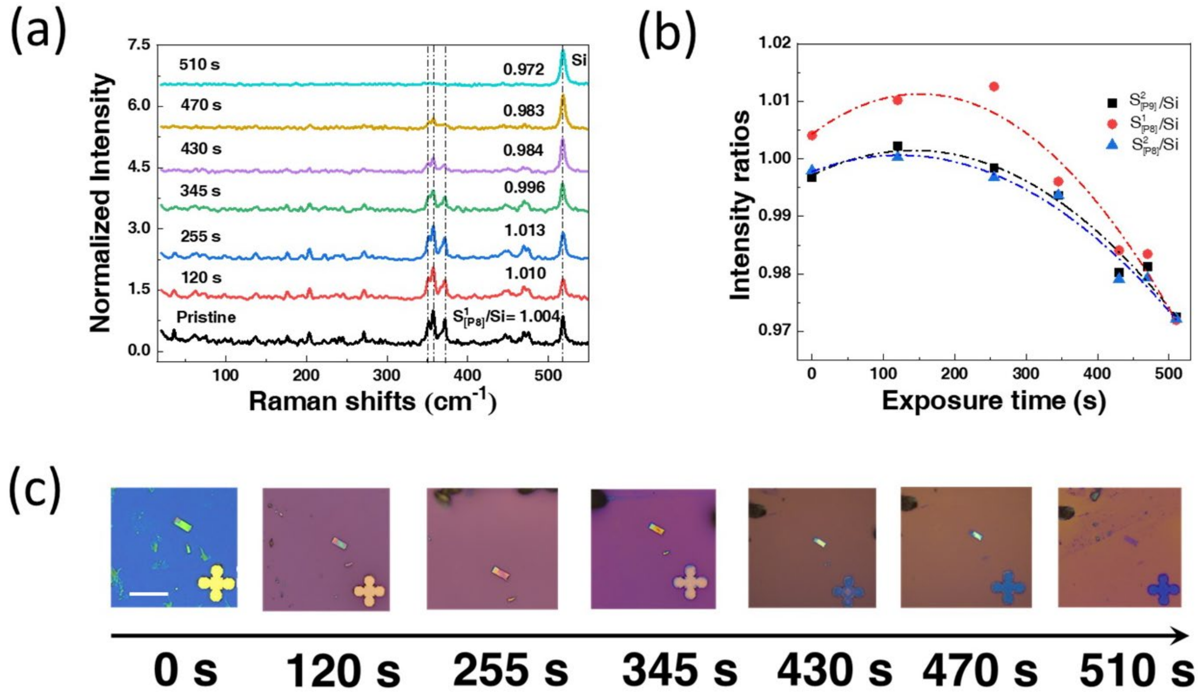

Figure S6. Ar^+ plasma exposure of the VP flake. a) The evolution of the Raman spectrum of a VP flake corresponding to the Ar^+ plasma exposure time. b) Ratios of the three main Raman peaks to the Si peak as a function of the plasma exposure time. c) The corresponding optical images as a function of the Ar^+ plasma exposure time.

As illustrated in **Figure S6**a, Raman modes in both the high-frequency and low-frequency ranges still exist visibly until a long Ar^+ plasma exposure (510 s for this flake). Beyond the crystal quality, the VP flake thickness strongly depends on the Raman spectra.[3] The three prominent localized intra-tube modes $S^2_{[P9]}$, $S^1_{[P8]}$and $S^2_{[P8]}$ are normalized to the Si peak for comparison, as shown in Figure S6b. In the process, the intensity ratio of $S^1_{[P8]}$ mode to Si peak increases slightly due to the removal of physically adsorbed H_2O/O_2 molecules.[4] Then, the intensity ratios keep decreasing to ~ 0.97, much lower than 1, suggesting that the intensity ratio can gauge the VP thickness (Figure S6c).[5] Similar trends can also be found in $S^2_{[P9]}$ and $S^2_{[P8]}$ modes. In addition, the low-frequency

Raman modes almost vanish after 430 s Ar^+ plasma, whereas the high-frequency modes are still visible. This is because the corresponding vibrations result from interlayer vdW interaction.[6]

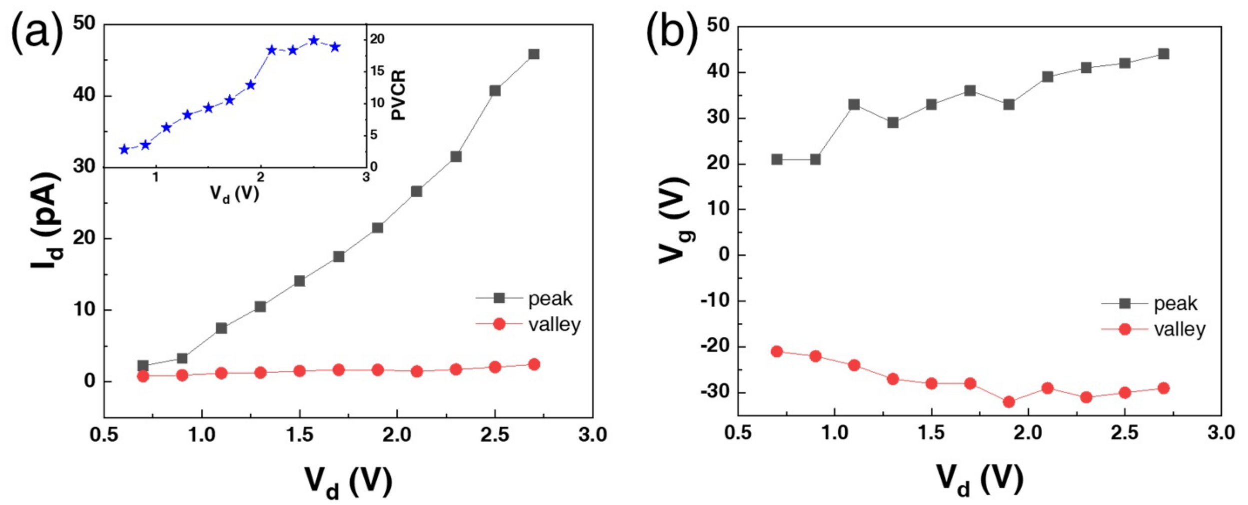

Figure S7. NDT characteristics with respect to various V_d. a) peak/valley current as a function of the applied V_d. The inset gives the values of the peak-valley current ratio (PVCR). b) peak/valley voltage as a function of the applied V_d.

Table S1. Comparison of the peak/valley current for various tunneling devices based on homojunctions

Materials	PVCR	T (K)	Device Architecture	Gate control	Light control
VP (this work)	20.35	300	NDT	yes	yes
WSe_2[7]	1.98	300	NDT	yes	yes
MoS_2[8]	1.1	10	NDR	yes	no
BP[9]	1.2	330	NDR	yes	yes
Si[10]	2	300	NDR	yes	no
Si[11]	10	300	NDT	yes	no
Si[12]	5.05	300	NDR	no	no
Gr[13]	1.3	1.4	NDR	yes	no

***VP**: violet phosphorus, **BP**: black phosphorus, **Gr**: graphene, **NDR**: negative differential resistance, **NDT**: negative differential transconductance*

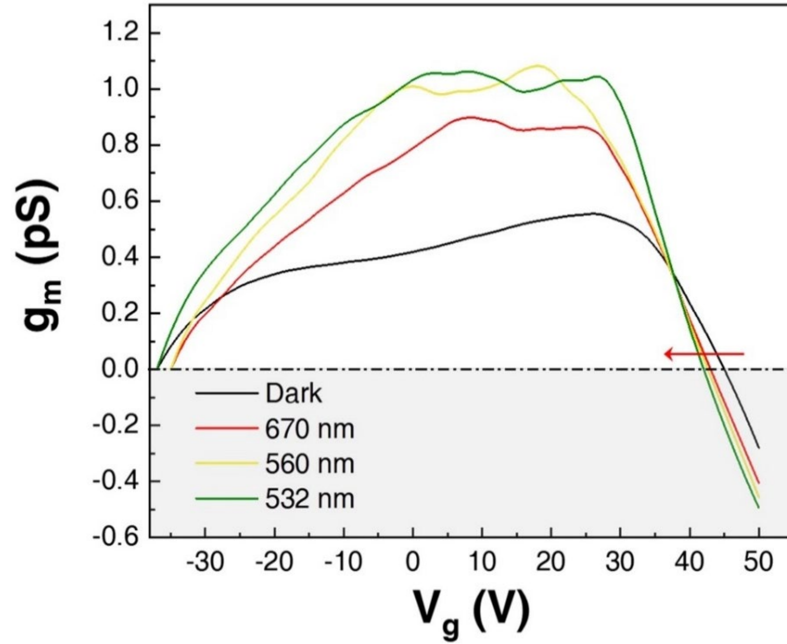

Figure S8. The relationship of transconductance (g_m) corresponds to gate bias (V_g) as a function of the wavelength of illumination light. Ultranarrow bandpass filters with different wavelengths (670, 560, and 532 nm) were employed to filter the incident light from the xenon light. The transparent efficiency of these filters can reach ~90% with the full bandwidth at half maximums of 10 nm.

References

[1] S. Lin, S. Liu, Z. Yang, Y. Li, T. W. Ng, Z. Xu, Q. Bao, J. Hao, C. S. Lee, C. Surya, F. Yan, S. P. Lau, *Adv. Funct. Mater.* **2016**, *26*, 864-871.

[2] F. Baumer, Y. Ma, C. Shen, A. Zhang, L. Chen, Y. Liu, D. Pfister, T. Nilges, C. Zhou, *ACS Nano* **2017**, *11*, 4105-4113.

[3] C. Lee, H. Yan, L. E. Brus, T. F. Heinz, J. Hone, S. Ryu, *ACS Nano* **2010**, *4*, 2695.

[4] H. Nan, Z. Wang, W. Wang, Z. Liang, Y. Lu, Q. Chen, D. He, P. Tan, Feng Miao, X. Wang, J. Wang, Z. Ni, *ACS Nano* **2014**, *8*, 5738-5745.

[5] C.-G. Andres, V. Leonardo, P. Elsa, O. I. Joshua, K. L. Narasimha-Acharya, I. B. Sofya, J. G. Dirk, B. Michele, A. S. Gary, J. V. Alvarez, W. Z. Henny, J. J. Palacios, S. J. v. d. Z. Herre, *2D Mater.* **2014**, *1*, 025001.

[6] P. H. Tan, W. P. Han, W. J. Zhao, Z. H. Wu, K. Chang, H. Wang, Y. F. Wang, N. Bonini, N. Marzari, N. Pugno, G. Savini, A. Lombardo, A. C. Ferrari, *Nat. Mater.* **2012**, *11*, 294-300.

[7] S. Seo, J. Koo, J.-W. Choi, K. Heo, M. Andreev, J.-J. Lee, J.-H. Lee, J.-I. Cho, H. Kim, G. Yoo, D.-H. Kang, J. Shim, J.-H. Park, *NPJ 2D Mater. Appl.* **2021**, *5*, 32.

[8] L.-N. Nguyen, Y.-W. Lan, J.-H. Chen, T.-R. Chang, Y.-L. Zhong, H.-T. Jeng, L.-J. Li, C.-D. Chen, *Nano Lett.* **2014**, *14*, 2381-2386.

[9] R. Cheng, L. Yin, R. Hu, H. Liu, Y. Wen, C. Liu, J. He, *Adv. Mater.* **2021**, *33*, 2008329.

[10] J. Koga, A. Toriumi, *IEEE Electron Device Lett.* **1999**, *20*, 529-531.

[11] C. Kim, Y. Lee, S. Lee, *J. Appl. Phys.* **2017**, *121*, 124504.

[12] M. Oehme, M. Sarlija, D. Hahnel, M. Kaschel, J. Werner, E. Kasper, J. Schulze, *IEEE Transactions on Electron Devices* **2010**, *57*, 2857-2863.

[13] B. Fallahazad, K. Lee, S. Kang, J. Xue, S. Larentis, C. Corbet, K. Kim, H. C. Movva, T. Taniguchi, K. Watanabe, L. F. Register, S. K. Banerjee, E. Tutuc, *Nano Lett.* **2015**, *15*, 428-33.